The Fibonacci Quasicrystal

Simon Groot

5710359

Supervisor: Cristiane de Morais Smith

Co-Supervisors: Jette van den Broeke and Sander Kempkes

Institute for Theoretical Physics

Utrecht University

June 13, 2018

Contents

Acknowledgements

I want to thank my supervisor Cristiane de Morais Smith for introducing me to this fascinating topic, and for all the time she spent guiding me through it. Even though it was sometimes difficult for me, I thoroughly enjoyed working on the subject. Thank you.

Furthermore, I want to thank my co-supervisors Sander Kempkes and Jette van den Broeke, not only for the many hours they spent explaining the material, correcting my work, and finding the mistakes in my code, but also for keeping the subject interesting through the many engaging discussions. I truly appreciate all the time and effort you spent. Thank you both.

Introduction

Ever since the discovery of Bragg diffraction early in the 20th century, scientists have been able to examine crystalline structures up to atomic precision. Since then, hundreds of thousands of crystals have been identified, and up until the early 1980's, all of them shared the property of periodicity. Scientists were therefore understandably surprised when in 1982 the first non-periodic crystal was discovered, and it took a long time for the scientific community to accept the discovery. This new class of crystals, named quasicrystals, turned out to be one of the most interesting subjects in the field of crystallography in the last 35 years. Some quasicrystals are extremely strong and do not corrode, which is convenient in cutting tools, while others have low heat conductivity and a low friction coefficient, making them very useful for heat insulating coatings.

Above all, quasicrystals are a very interesting mathematical subject. The theory of filling a space aperiodically had already been developed in the years before the discovery, and could readily be applied on the new crystals. Furthermore, it was proven that quasicrystals can be generated using regular crystals in higher dimensions, see Ref. [1]. In recent experiments, 1D quasicrystals have also been shown to exhibit new types of topological phases, previously only attributed to higher dimensional systems, see Ref. [2].

In this thesis, we will focus our attention on one specific quasicrystal called the Fibonacci quasicrystal. Since it is one dimensional it is one of the easiest quasicrystals to understand and analyse. Nevertheless, it will turn out to have some very interesting mathematical properties. In particular, it has a recursive structure in its energy spectrum.

In the first section, we will provide an introduction to quasicrystals and explain why for many years physicists dismissed their existence. We will furthermore provide a proof for a central theorem in crystallography, called the *Crystallographic Restriction Theorem*, which quasicrystals violate. Finally we will explain how we can generate quasicrystals from higher dimensional regular crystals.

In the second section, we will follow a 2016 article by Macé et al. about the Fibonacci quasicrystal, see Ref. [3]. In this article, an approximation for the Hamiltonian is used to predict a property of the energy spectrum. A connection is then made from the 1D Fibonacci quasicrystal to the 2D regular crystal from which it can be generated. By using this connection, a

symmetry is found in the localization of the eigenstates of the quasicrystal.

In the third section, we will numerically verify the analytical predictions made in the second section. We will solve the Schrödinger equation numerically on areas designed to simulate the Fibonacci quasicrystal. On a 1D area, we will find a remarkable agreement between the theoretical predictions and the numerical results. We will perform the same numerical calculation on a 2D area, which is more representative of a potential experiment. We will find the 2D simulation to be less accurate, but to still possess the same symmetries as the theoretical model at first order.

In the fourth section, we will discuss a relatively new technique in microscopy called *Scanning Tunneling Microscopy*. These microscopes allow us to position individual atoms on a surface with atomic precision. This has enabled scientists to design surfaces that very accurately simulate any type of crystal lattice in two dimensions. This technique has therefore frequently been used to measure properties like the energy spectrum and the localization of the eigenstates for all kinds of crystal lattices.

In the fifth section, we will take a look at two experiments that employ this very technique. The first experiment by Gomes et al. aims to design a surface which simulates the exciting new material graphene, see Ref. [4]. Atoms are placed on a surface in a triangular pattern, in order to replicate the hexagonal structure of graphene, and the electronic properties of the surface match with those of graphene. The second experiment by Collins et al. actually studies a quasicrystal, though not the Fibonacci quasicrystal. It examines the electronic properties of a 2D quasicrystal called the Penrose tiling, see Ref. [5]. It finds a very similar property in the localization of the eigenstates to the predictions we made about the Fibonacci quasicrystal, further supporting our findings.

1 Quasicrystals

Before 1982, the existence of quasicrystals was unknown to physicists. Regular crystals, however, were already a well-known subject at that time, and in order to understand quasicrystals it is necessary to first understand the basic properties of regular crystals.

It took until the first X-ray diffraction experiment in 1912 for physicists to establish a proper definition of a *crystal*. These experiments revealed that many solid materials possess symmetries in their atomic structure. One definition of crystals at that time reads: *A solid composed of atoms arranged in a pattern periodic in three dimensions*, see Ref. [6]. The structure of a crystal can be visualized using a periodic array of points called a *lattice*. An important consequence of the periodicity of the lattice is the *Crystallographic Restriction Theorem*. This theorem states that a periodic lattice can only have 2-, 3-, 4- or 6-fold rotational symmetry. We will provide a short proof of this theorem.

Assume we have a periodic lattice which is invariant when rotated by an angle $\theta = 2\pi/n$ around any lattice point, with n a positive integer. Consider a line of lattice points along which the crystal is periodic, with a certain lattice constant a. We will look at three consecutive lattice points **A-O-B** (see Fig. 1). We can now rotate **A** and **B** by θ to the lattice points **A'** and **B'**. The line through **A'** and **B'** is parallel to our original line. It should therefore also be periodic with lattice constant a. It follows that the distance s between **A'** and **B'** has to obey $s = ma$, with m an integer. From geometry we can find s to be $2a\cos\theta$. So, the obtained relation is:

$$\cos\theta = \frac{m}{2} \quad \text{for integer m,}$$
$$\theta = \frac{\pi}{3}, \frac{\pi}{2}, \frac{2\pi}{3} \text{ or } \pi \tag{1}$$

This corresponds to 6-,4-,3- and 2-fold rotational symmetry respectively, therefore proving the theorem. The trivial solution $\theta = 2\pi$ is usually not considered.
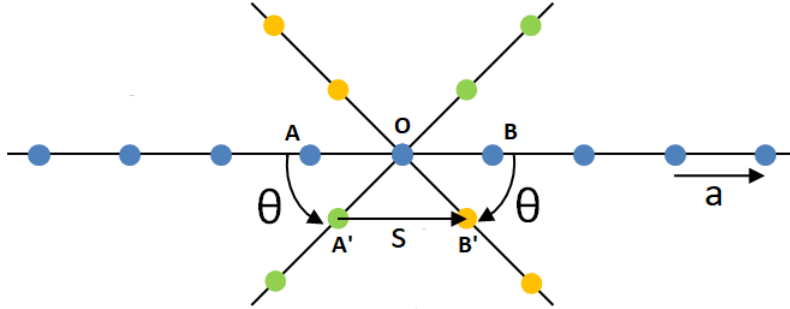
Figure 1: A periodic lattice invariant under a rotation of θ. Consequently, the distance s between the points **A'** and **B'** has to be equal to an integer times the lattice constant a. This restricts θ to $\pi/3, \pi/2, 2\pi/3$ or π

We can subsequently describe a periodic lattice as a constantly repeating cell, usually called a *unit cell*. It is important to note that this unit cell has to fill the space without gaps by repeating itself. The unit cell must have the same rotational symmetry as the lattice itself. So, the restriction theorem also dictates that the only unit cells that can fill the entire space continuously are 2-,3-,4- or 6-fold rotationally symmetric. Therefore, there will only be a finite number of distinct unit cells. The lattices generated by these unit cells are called the *Bravais-lattices*. All of the 2-dimensional Bravais-lattices are depicted in Fig. 2.
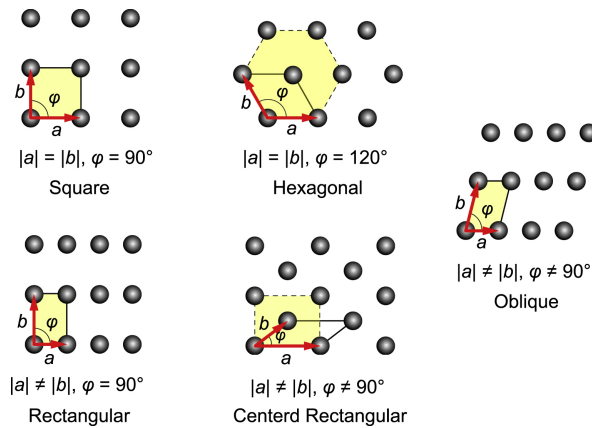

Figure 2: The 2-dimensional Bravais-lattices with the corresponding unit cell. They are translationally invariant in two directions and have 2-,3-,4- or 6-fold rotational symmetry. In 3 dimensions there are 14 Bravais-lattices and in 1 dimension there is only 1. The figure has been extracted from Ref. [7].

This brings us to the discovery of quasicrystals in 1982. A diffraction ex-

periment conducted by Dan Shechtman on an aluminium-manganese alloy revealed a lattice that appeared to have 10-fold rotational symmetry (see Fig. 3), although it later turned out to be 5-fold, see Ref. [8]. As we just established, there is no unit cell with 5-fold rotational symmetry, which means that this lattice cannot be constructed by a repeating unit cell. Consequently, although it has rotational symmetry, this lattice cannot be periodic. This was previously thought to be impossible and, a new definition of crystals had to be introduced. This new definition contained both the periodic and the aperiodic crystals or quasicrystals. Shechtman would later receive a Nobel prize for his findings.
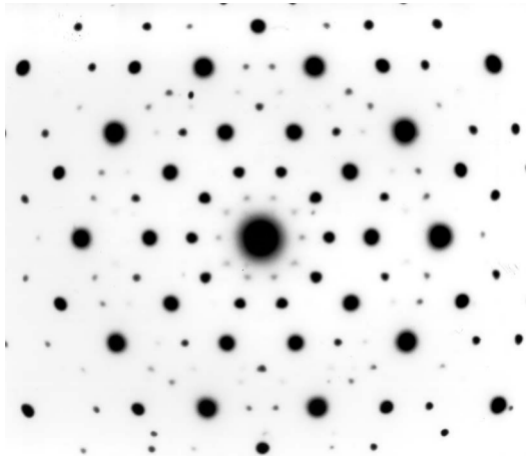

Figure 3: The original diffraction pattern obtained in Shechtman's experiment. It clearly possesses 5-fold rotational symmetry, which was previously thought to be impossible for crystals. This figure has been extracted from Shechtman's 2011 Nobel Lecture.

Interestingly enough, all quasicrystals can be described as the projection of a higher dimensional periodic lattice. For a rigorous mathematical proof of this claim see Ref. [1]. To illustrate this, we will discuss a famous example of creating a one dimensional quasicrystal, using a periodic two dimensional lattice. Consider a square lattice in two dimensions, with points on every position (m, n) for integer m and n. A line going through the origin with irrational slope will never intersect with any of the other lattice points. If we then project every lattice point within a certain range of this line onto it, we obtain a sequence of points on the line (see Fig. 4). This sequence of points is a one dimensional quasicrystal. Furthermore, if we pick the slope to be exactly $1/\tau$, with $\tau = (1 + \sqrt{5})/2$ the golden ratio, we obtain the so-called *Fibonacci* quasicrystal. We will discuss the main features of this crystal in
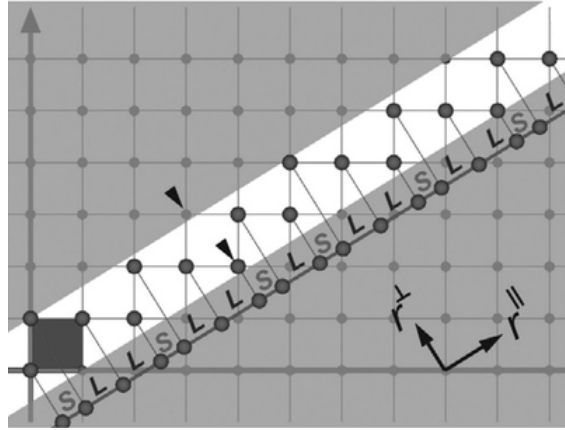
the next section.

Figure 4: The construction of a 1D quasicrystal by projecting a 2D periodic lattice onto a line with irrational slope. The resulting sequence of points is a quasicrystal. The line has been shifted outside the range for clarity, but this does not affect the sequence. Note that the range around the line is determined by placing a square of unit length at the origin and projecting its size along the line.

2 Energy spectrum of the Fibonacci quasicrystal

2.1 Construction of the Fibonacci quasicrystal

In this section we will further investigate the Fibonacci quasicrystal. An alternative way to construct it is by making use of the Fibonacci word. We use this terminology to distinguish from the Fibonacci sequence, which is the famous sequence of numbers, and the Fibonacci chain, which denotes the chain of sites that can be generated with the Fibonacci word. There are many ways to construct the Fibonacci word. One of them is by repeated substitution. We start off with one S and repeatedly substitute $S \to L$ and $L \to LS$ (see Table 1). One way to think of this sequence is in terms of rabbits. S denoting a small rabbit and L a large one. In every new generation small rabbits will grow up ($S \to L$) and large rabbits will reproduce ($L \to LS$). An alternative name for this sequence is therefore the *rabbit sequence*. If we now take the limit of the number of generations to infinity, we obtain the Fibonacci word.

Number of letters	Generations of the Fibonacci word
1	S
1	L
2	LS
3	LSL
5	LSLLS
8	LSLLSLSL
13	LSLLSLSLLSLLS
21	LSLLSLSLLSLLSLSLLSLSL

Table 1: The first few generations of the Fibonacci word. The left-hand side denotes the number of letters in the generation, and follows the Fibonacci sequence.

From this sequence we can construct a quasicrystal by associating L and S with the distances between sites on a 1-dimensional lattice, L being a long distance and S being a short distance. The energy spectrum of this quasicrystal will turn out to have some interesting properties, as was shown in Ref. [3]. In the following calculations, we will approximate the infinite Fibonacci quasicrystal by looking at a periodic system, with the n-th generation of the finite Fibonacci chain as a unit cell. This system is called the n-th approximant.

We consider a tight-binding Hamiltonian for this crystal

$$H = \sum_i t_i(|i\rangle\langle i+1| + |i+1\rangle\langle i|), \tag{2}$$

where t_i is the hopping constant between site i and $i+1$, depending on the distance between the sites. The constant can therefore take on two values, t_s (where the subindex s denotes strong, corresponding to S) and t_w (where the subindex w denotes weak, corresponding to L). The structure of the Hamiltonian depends on the single parameter $\rho = t_w/t_s$. Changing the hopping constants without changing the ratio between them only scales the energy values.

As L appears more frequently in the Fibonacci word than S, the same goes for t_w in comparison to t_s. The ratio of their frequency will actually converge to the golden ratio as we increase our approximant in size. We will provide a quick proof for this claim. Suppose that, for a chain of n generations C_n, we have the number of times that t_s and t_w occur $N_n(t_w) = F_{n-1}$ and $N_n(t_s) = F_{n-2}$ respectively, with F_n the n-th Fibonacci number. If we now substitute $S \to L$ and $L \to LS$ to obtain C_{n+1}, we find

$$N_{n+1}(t_w) = N_n(t_w) + N_n(t_s) = F_{n-1} + F_{n-2} = F_n$$
$$\text{and} \quad N_{n+1}(t_s) = N_n(t_w) = F_{n-1}. \tag{3}$$

It is easy to see that C_2 satisfies our initial assumption. So, by induction,

$$\forall n > 2, \ N_n(t_w) = F_{n-1} \quad \text{and} \quad N_n(t_s) = F_{n-2}. \tag{4}$$

For the infinite Fibonacci chain, the ratio between the frequencies will therefore be

$$\frac{N_\infty(t_w)}{N_\infty(t_s)} = \lim_{n\to\infty} \frac{F_{n-1}}{F_{n-2}} = \frac{1+\sqrt{5}}{2}, \tag{5}$$

which is the golden ratio.

2.2 Molecules and Atoms

We can give a physical interpretation to the system by associating two strongly connected sites with a diatomic molecule, and a site with weak connections to either side with a single atom (see Fig. 5).
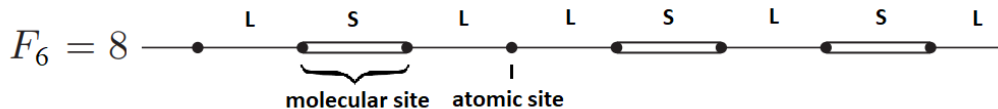
Figure 5: The unit cell of the sixth approximant of the Fibonacci chain. The bonds follow the pattern of the Fibonacci word (see Table 1). The double bonds denote a strong hopping t_s and the single bonds a weak hopping t_w. We can interpret two strongly bonded sites as a diatomic molecule and a site with weak bonds to either side as a single atom. This figure has been extracted from Ref. [3] and has been modified for convenience.

We will consider the atomic and molecular energy levels separately, and later combine them. There can either be one or two molecules between two atoms. We can therefore approximate the coupling between two nearest atoms with one of two values, which we will call t'_w and t'_s. We can construct a new lattice by carrying out these approximations for every atomic site (see Fig. 6). In fact, what we end up with is again an approximant of the Fibonacci chain, but three iterations back. In other words, if we have a chain of n iterations C_n, then the atomic energy levels are described by the Hamiltonian of C_{n-3}. This transformation is called the *atomic deflation*.
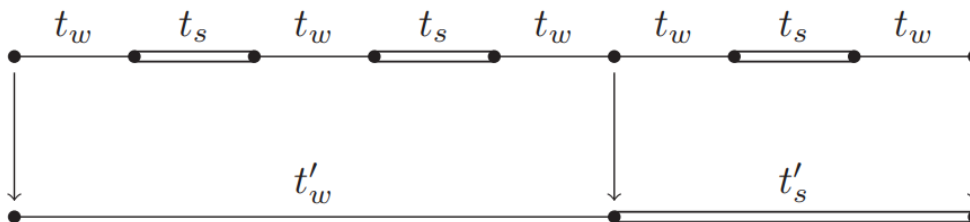

Figure 6: Atomic deflation of the sixth approximant. The unit cell has been shifted in order to make the approximation clearer. We approximate the atomic energy levels by looking at the chain C_{n-3}. In this case the sixth approximant is transformed to the third. Because of periodicity, the last site is the same as the first one, which is why there seem to be nine sites in the figure instead of eight. This figure has been extracted from Ref. [3].

This method also works for the molecular energy levels. There will be either zero or one atom in between molecules, again resulting in two distinct coupling constants. However, this time we find the chain describing the molecular levels to be equal to C_{n-2} (see Fig. 7). Similar to before, this

transformation is called the *molecular deflation*. Since the two orbitals located on a diatomic molecule can either be in a bonding or an anti-bonding state, we need to shift H_{n-2} by $\pm t_s$ to obtain the energy levels of the molecular sites in our original chain.
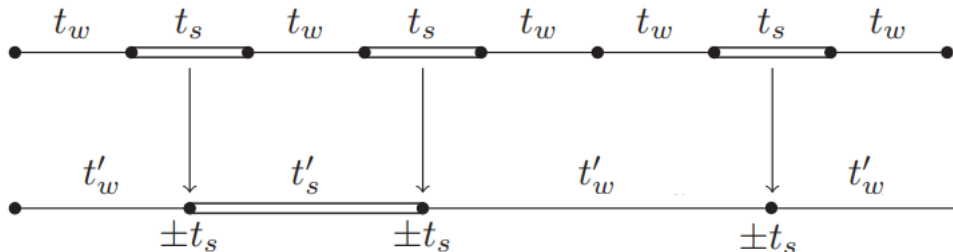

Figure 7: Molecular deflation of the sixth approximant. The unit cell has again been shifted for clarity. The molecular energy levels can be approximated by looking at the chain C_{n-2}. In this case the sixth approximant is transformed to the fourth. Because of periodicity, the last site is the same as the first one, which is why there seem to be nine sites in the figure instead of eight. This figure has been extracted from Ref. [3].

Now that we have the energy levels for the molecular and atomic sites, we can write the Hamiltonian of our original chain as:

$$H_n = (zH_{n-2} - t_s) \oplus (\bar{z}H_{n-3}) \oplus (zH_{n-2} + t_s) + \mathcal{O}(\rho^4), \qquad (6)$$

where $z = \rho/2$ and $\bar{z} = \rho^2$ are scaling factors, with $\rho = t_w/t_s$. Their value is derived in Ref. [9]. This approximation is exact in the limit $\rho \ll 1$. We can give a minimal condition for the validity of this approximation, by requiring ρ to be sufficiently small such that the different parts of the Hamiltonian do not overlap, as was proposed in Ref. [10]. To formulate this mathematically, we denote the width of the energy spectrum of C_n by Δ_n. The distance between the two molecular parts of the Hamiltonian is $2t_s - z\Delta_{n-2}$. The atomic part of the Hamiltonian needs to fit in between the two molecular parts, so our condition becomes

$$\bar{z}\Delta_{n-3} \leq 2t_s - z\Delta_{n-2}. \qquad (7)$$

2.3   Energy spectrum and LDOS

The structure of the energy spectrum now starts to become clear. We see in Eq. 6 that the spectrum can be decomposed into three main clusters, a

13

bonding and anti-bonding molecular cluster, and the atomic cluster. Since these are all scaled energy spectra of previous iterations of our Fibonacci chain, we can again decompose each cluster into three smaller clusters, and so on (see Fig. 8). Therefore, the energy spectrum has a recursive, Cantor set-like description.
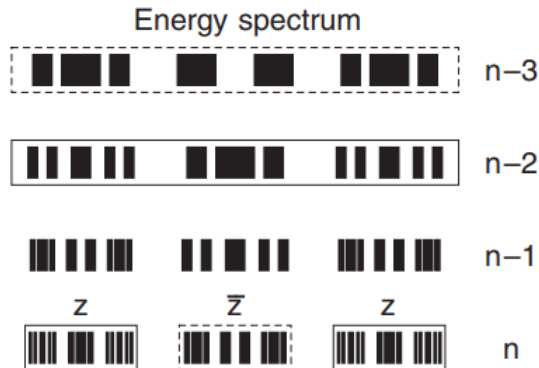

Figure 8: Energy spectrum of C_n. The top two rows show the spectra of the chains C_{n-3} and C_{n-2}. We can subsequently construct the spectrum of C_n on the bottom row by combining these two spectra. This figure has been extracted from Ref. [3].

Finally, we can also observe this triple structure when looking at the eigenfunctions corresponding to these energy levels. In order to reveal this, we first need to rearrange the sites in a certain way. We want to group the sites together such that we have two equally sized clusters of molecular sites and one of atomic sites, similar to the eigenenergies.

For any chain C_n with $n > 3$, the number of atomic sites is equal to $N_A = F_{n-3}$. Since the total number of sites of C_n is F_{n-1}, it follows that the number of molecular sites is $N_M = F_n - F_{n-3} = 2F_{n-2}$. Hence, our molecular groups will both have to contain F_{n-2} sites, and our atomic group F_{n-3}.

Here we recall that we can construct the Fibonacci quasicrystal using the projection method, as was discussed in the previous section. We can obtain any finite chain C_n by only taking the first F_n sites generated by the projection. If we take a close look at the construction of a chain C_n by this method, we notice that there is a very natural way to divide the sites into the three desired clusters. Within the projection range, the molecular sites are located near the edges of the range, while the atomic sites are clustered in the centre (see Fig. 9). If we now number these sites horizontally from bottom to top,

the first F_{n-2} are molecular, then we have F_{n-3} atomic sites, and finally we have F_{n-2} molecular sites again. Numbering the sites in this manner is called *conumbering*. The conumbers of a chain C_n follow the pattern of

$$c(i) = iF_{n-1} \mod F_n, \tag{8}$$

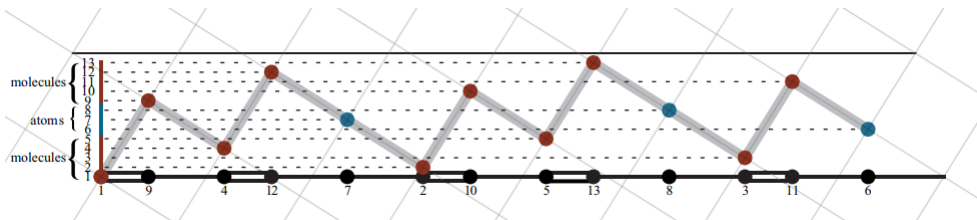where $c(i)$ is the conumber corresponding to site i.

Figure 9: The first 13 sites resulting from the projection method, equivalent to C_7 when using the rabbit sequence (see Table 1). If we look along the projection range, we notice that the molecular sites are located near the top and bottom, while the atomic sites are clustered in the centre. We number them horizontally from top to bottom, which is called *conumbering*. This figure has been extracted from Ref. [3].

This division is similar to the atomic and molecular deflation, where we approximate C_n by looking at the atomic or molecular sites separately. Crucially, since the deflated chains are again Fibonacci chains, the individual atomic and molecular clusters are also Fibonacci chains, just three and two generations back respectively. We can therefore again divide every cluster into another two molecular and one atomic cluster, and so on. This is very similar to the way we decomposed the energy spectrum.

Finally, we can observe this similarity by looking at the eigenfunctions corresponding to the eigenenergies, and calculating on which sites they are localized. To show this, we perform a periodic tight-binding calculation for the chain C_{11}, with $F_{11} = 89$ sites. The resulting eigenvectors tell us the localization of this state on every site, i.e. the first component of the first eigenvector tells us the localization of the first eigenstate on the first site. We can use this to calculate the local density of states (LDOS) of the electrons,

$$\text{LDOS}(r, \epsilon) = \sum_n |\Phi_n(r)|^2 \delta(\epsilon - \epsilon_n), \tag{9}$$

with Φ_n the eigenstate corresponding to the n-th eigenenergy ϵ_n. If we then rearrange the site according to their conumbers, the recursive structure re-

15

veals itself, see Fig. 10. As is to be expected, the eigenfunctions corresponding to the molecular energy levels are highly localized on the molecular sites, on the edges. The eigenfunctions corresponding to the atomic energy levels are, however, highly located on the molecular sites, in the centre. Since the clusters on the x-axis and the energy spectrum on the y-axis both have a recursive structure, the figure also has this property. It consists of five main squares, each of which contains a similar, but smaller figure, and so on. The figure is also invariant under exchange of the position- and energy-axes.
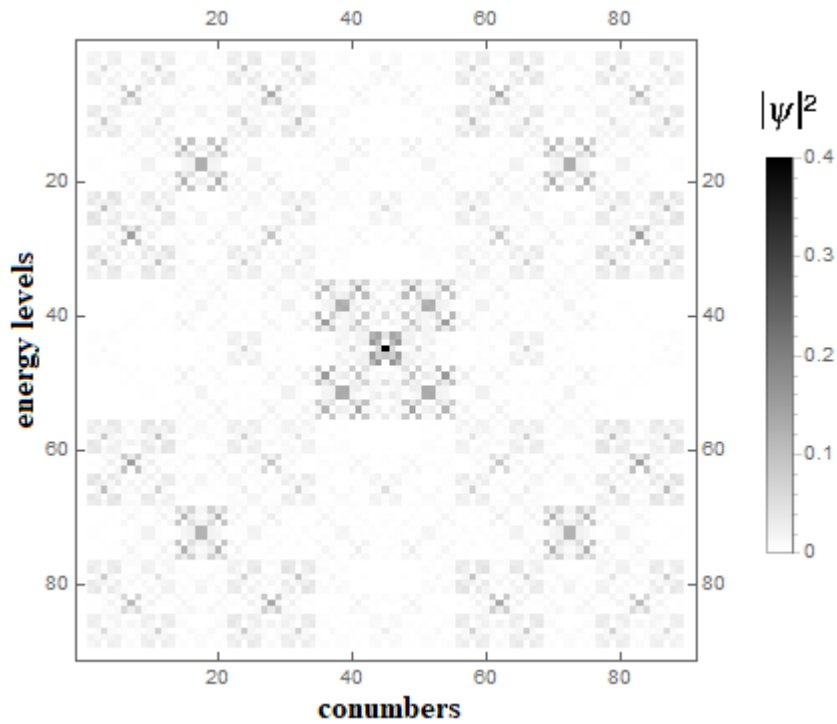

Figure 10: LDOS of C_{11}, using a tight-binding approximation. The figure shows the localization of the eigenfunctions of the chain on its sites. On the y-axis we have the energy levels to which the eigenfunctions correspond, and on the x-axis we have the rearranged sites, according to their conumbers.
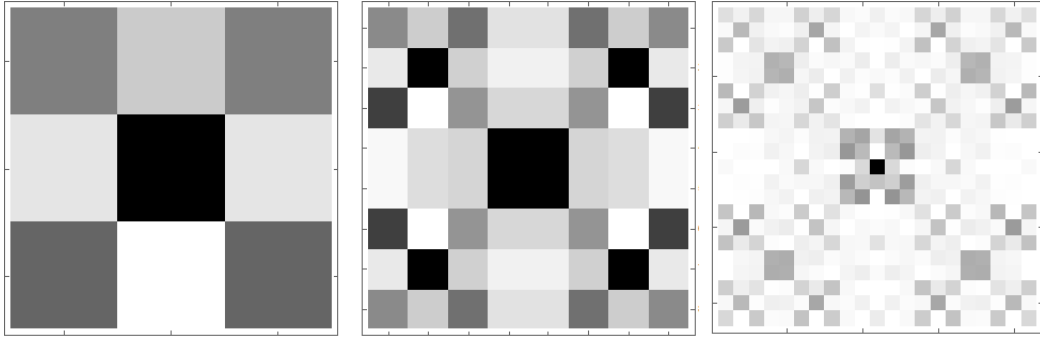
16

Figure 11: The geometrical construction of the LDOS. From left to right, we have shown the LDOS for C_4, C_6, and C_8.

3 Comparison to numerical calculations

Now that we have discussed the theoretical properties of the Fibonacci quasicrystal, it will be interesting to see whether we can obtain these same properties numerically. In this section, we will discuss the results that were obtained by solving the Schrödinger equation numerically on a region that simulates the one-dimensional Fibonacci quasicrystal.

In the previous section we took a mathematical approach in order to make predictions about the 1D Fibonacci quasicrystal. In particular, we predicted a recursive triple structure for the energy spectrum, where it could be continuously divided into two molecular parts at the edges and an atomic part in the centre. Furthermore, we predicted that see the same structure should be observed when looking at the LDOS with the sites rearranged in a way that the molecular sites are located at the edges and the atomic sites in the centre. We now want to verify whether we can confirm this result in a numerical calculation.

3.1 Construction of the lattice

For this, we first need to construct a region that simulates the 1D Fibonacci quasicrystal. We start off with the Fibonacci word of a certain generation n, which consists of F_n letters. In the theoretical model, the letters of the Fibonacci word correspond to the distance between neighbouring lattice sites. In turn, this determines a certain hopping between the two sites. In the numerical model the sites are evenly spaced, but we simulate the two different hopping parameters by introducing two different height potentials of a certain width P_{width}, which we will denote V_L and V_S, corresponding to the hopping parameters t_w and t_s respectively. We then place these potentials on a one dimensional region with length F_n, following the order of the Fibonacci word, i.e. we place a potential of height V_L at the position $x = 0$, V_S at $x = 1$, up until the last potential at $x = F_n - 1$. In the mathematical derivation, we approximated the Fibonacci quasicrystal with a periodic unit cell of the n-th generation chain C_n. We replicate this approximation by introducing periodic boundary conditions to our region. In order to do this, we add a potential V_L at $x = F_n$, see Fig. 12. Our region now consists of F_n enclosed sites, and we can impose the periodic boundary conditions by "gluing" the potential V_L at $x = F_n$ to the V_L at $x = 0$.
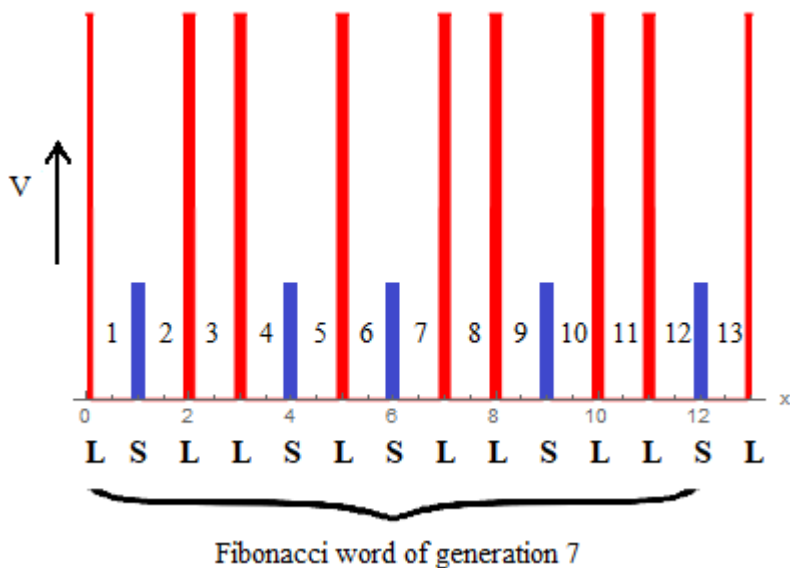
Figure 12: The region that approximates the lattice of C_7. We have a one dimensional space with potentials V_L, depicted by the red bars, and V_S, depicted by the blue bars. The first 13 potentials follow the pattern of the 7-th generation Fibonacci word. We then add one more potential V_L at the end. As a result we obtain a region with $F_7 = 13$ sites, just like in the chain C_7. The sites are marked with the numbers 1 through 13.

In theory, we now have a good approximation of the theoretical lattice. In practice, however, we need to make one more adjustment. When the potential height V_S is small compared to V_L, it allows the high-energy electrons to also "sit" on top of the small potential V_S in between molecular sites. As a result, the effective size of the molecular sites is larger than that of the atomic sites, which lowers the on-site energy of the molecular sites. In the theoretical model we do not run into this problem, since the electrons are mathematically confined to the discrete sites, and cannot "sit" on top of a bond in between sites. Depending on the potentials, this can cause the high molecular energy levels to mix with the atomic energy levels, or in some cases they can even be lower than the atomic energy levels. To solve this, we artificially shrink the molecular sites by a certain factor $0 < \gamma \leq 1$, such that their effective size is comparable to the size of the atomic sites.

3.2 Eigenenergies and eigenfunctions

We now have everything to make a proper approximation of the Fibonacci quasicrystal, and check whether we can find any of the previously determined

19

properties. We have calculated the energy-eigenvalues for a region with $F_{10} = 55$ sites in Fig. 13. The energy spectrum clearly divides into two molecular groups of $F_8 = 21$ eigenvalues at the top and bottom, and an atomic group of $F_7 = 13$ eigenvalues in the middle. Moreover, we can actually see the recursive structure, as the triple division is still apparent after zooming in twice on the bottom molecular energy levels. Furthermore, we would expect the energy spectrum to be symmetric, but the top higher energy levels seem to be more spaced out than the lower energy levels. We suspect the reason for this to be that the ratio between potential and energy value decreases for higher energy levels. Therefore the higher energy levels are affected less by the potentials than the lower ones.
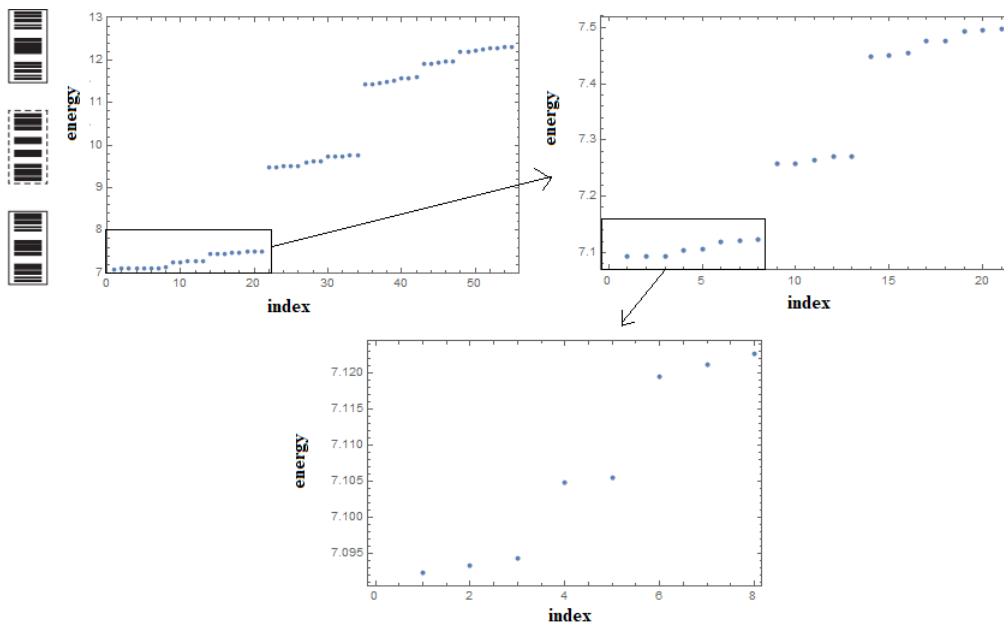

Figure 13: The eigenvalues obtained by numerically solving the Schrödinger-equation on a region with $F_{10} = 55$ sites. We used the potential heights $V_L = 100$ and $V_S = 30$, the potential width $P_{width} = 0.2$, and the molecular site shrinking factor $\gamma = 0.92$. On the left, the theoretical structure of the energy spectrum was added from the previous section. The first figure to the right of this is the set of the first 55 energy eigenvalues. The two figures after this, zoom in consecutively on the part of the set highlighted in the black boxes. The three-part division is noticeable until two levels deep, revealing the recursive structure of the energy spectrum.

Furthermore, we have calculated the LDOS for the eigenfunctions corre-

sponding to these energy levels. In the numerical approximation, we use

$$\text{LDOS}(r, \epsilon) = \sum_n |\Phi_n(r)|^2 f(\epsilon \mid \epsilon_n, \sigma), \tag{10}$$

where we have introduced a broadening $f(\epsilon \mid \mu, \sigma)$ with mean μ and standard deviation σ for the numerical approximation, instead of the δ-function in the theoretical model. This allows for some overlap between the energy levels. In our case, we used a normal distribution for the broadening, where σ is determined by hand based on the spacing of the energy spectrum. If we now look at the LDOS, we already see a clear split in the eigenfunctions, see Fig. 14. The middle eigenfunctions seem to be dominant on the atomic sites, while the outer eigenfunctions are more prominent on the molecular sites.
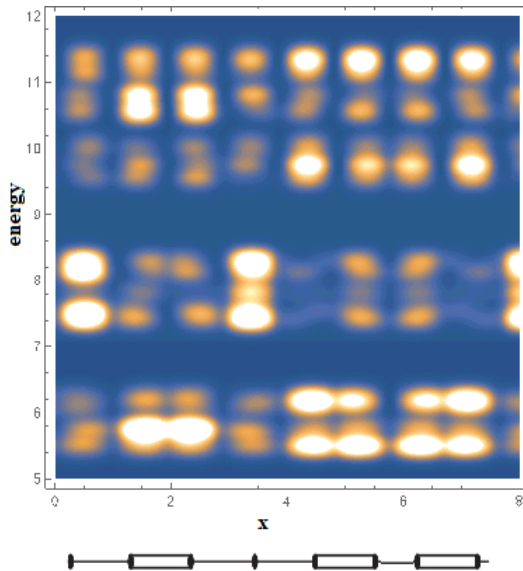

Figure 14: The LDOS for the first eight sites of C_{55}. To make the figure clearer, we used different parameters than in Fig. 13. The potential heights are $V_L = 50$ and $V_S = 25$, the potential width is still $P_{width} = 0.2$, the molecular site shrinking factor is $\gamma = 0.94$, and we used $\sigma = 0.1$.

If we then rearrange the sites according to their conumbers and plot the LDOS, we obtain Fig. 15. Again, we clearly see the three-part division, where the molecular eigenfunctions are localized on the molecular sites in the corners, and the atomic eigenfunctions are localized on the atomic sites in the centre. On top of this, if we look closely, we see that these 5 regions subdivide two more times, showing the same recursive property as the energy spectrum.
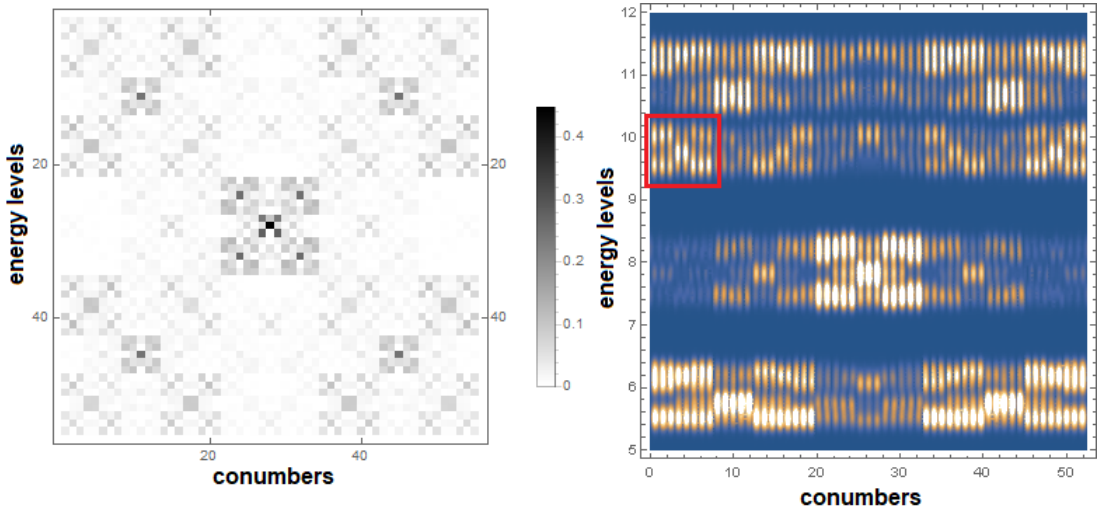
Figure 15: The LDOS obtained by a tight-binding calculation for 55 sites (left), compared to the LDOS obtained by numerically solving the Schrödinger equation for a region with $F_{10} = 55$ sites. Because the molecular sites are shrunk by a shrinking factor γ, the x-axis does not actually run from 0 to 55 for the numerical figure, but rather stops at 52.48. The parameters are the same as in Fig. 14. For these particular values, we can see the recursive structure multiple levels deep. The main plot divides into 5 regions, which again divide into 5 regions, and in the top left and top right we can see some of these regions divide into 5 regions again, as indicated by the red box.

3.3   2D lattice

As a final comparison, we will examine the same results for a two dimensional region. This will be more representative of the results of a potential experiment. We construct the 2D region that simulates the Fibonacci quasicrystal similar to the 1D region. However, now the region has a width in addition to its length of F_n. We then extend all of the potentials along the width of the region to the edges to enclose all the sites, see Fig. 16. We have chosen the width to be 0.8 such that, if you take the space occupied by potentials into account, every site is a square with side length 0.8. Furthermore, in addition to the periodic boundary conditions along the short edges, we impose Dirichlet boundary conditions along the long edges, meaning that the eigenfunctions should be zero at $y = \pm 0.4$. Finally, we need to artificially shrink the molecular sites again, for the same reasons as mentioned before.
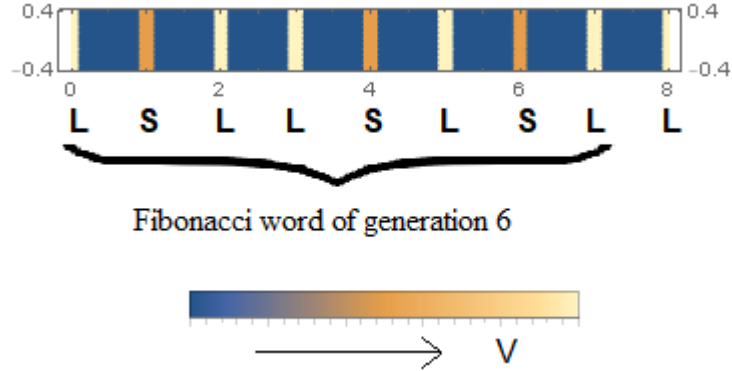
22

Figure 16: The region that approximates the lattice of C_6 in two dimensions. The potentials are placed in the same way as the one dimensional case, and are then extended to the edges.

If we now calculate the energy eigenvalues and the LDOS for the rearranged sites, we obtain Fig. 17 and Fig. 18, respectively. As expected, the energy spectrum divides into three parts. However, it is hard to see any further divisions, unlike the one dimensional case. For different parameter values, it is possible to make one more division observable, but in general the two dimensional approximation does not demonstrate the recursive structure as clear as the one dimensional case does. Furthermore, in the LDOS figure, the primary and secondary divisions are apparent. However, the third division is hard to see, unlike the one dimensional case.
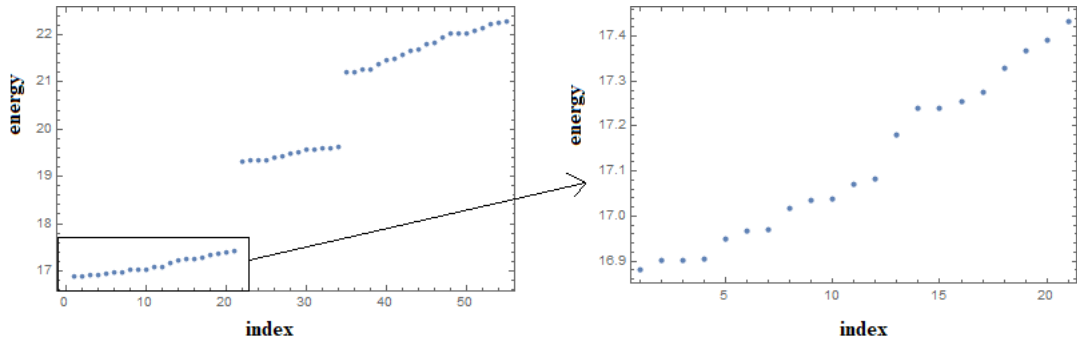

Figure 17: The eigenvalues obtained by numerically solving the Schrödinger-equation on the two dimensional region with $F_{10} = 55$ sites. We used the parameter values as in Fig. 13, $V_L = 100$ and $V_S = 30$, the potential width $P_{width} = 0.2$, and the molecular site shrinking factor $\gamma = 0.92$. The first figure shows the first 55 energy eigenvalues. The second figure zooms in on the first 21 energy eigenvalues.
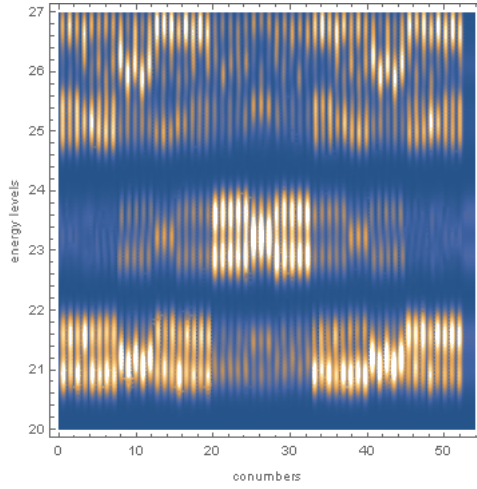
Figure 18: The LDOS obtained by numerically solving the Schrödinger equation for the two dimensional region with $F_{10} = 55$ sites. We used the same parameters as in Fig. 15, except for σ, which we had to change since the energy levels are more spaced out . The potential heights are $V_L = 50$ and $V_S = 25$, the potential width is $P_{width} = 0.2$, the molecular site shrinking factor is $\gamma = 0.94$, and we used $\sigma = 0.2$.

4   Scanning Tunnelling Microscopy

Now that we have made theoretical predictions about the Fibonacci quasicrystal, and have supported those predictions by numerical calculations, the final step would be to experimentally verify our findings. This could be done nowadays by employing a technique called *Scanning Tunnelling Microscopy* (STM). This specific type of microscope falls within the broader category of incredibly accurate microscopes called *Scanning Probe Microscopy*; however we will focus our attention on STM, as this is the technique that is most useful for our subject. In this section we will explain how it works, and how it can be applied to investigate our predictions.

In order to test our predictions, we need to be able to analyse a lattice with an atomic precision, i.e. a resolution of order 1 Ångström. Before the invention of STM, this precision could only be achieved using a *Transmission Electron Microscope* or TEM because optical microscopes are limited by the wavelength of the light they emit, which is generally orders of magnitude greater than 1 Å. A TEM measures the transmission of electrons through a very thin sample, usually of the order of 100 nm. This technique is useful when looking at the composition and thickness of materials, but not necessarily when trying to determine the structure on the surface of the sample. As we will explain later, we do need a microscope that can do this to accurately test our predictions.

This is where we can use an STM. These types of microscopes are based on the quantum mechanical phenomenon called quantum tunnelling. The idea is to use a fine metal tip as a probe, with which we can map the surface structure. First we apply a voltage difference between the surface of the sample and the metal tip. If we then bring the metal tip close enough to the surface, electrons will be able to tunnel through the vacuum in between the tip and the sample, causing a very small current to flow through the metal tip, see Fig. 19. As the distance between sample and tip decreases, the current will strictly increase. Therefore, every current corresponds to a certain tip-sample distance. As we will show, a deviation of the size of an atom will already noticeably affect the tunnelling current, giving us the required resolution.
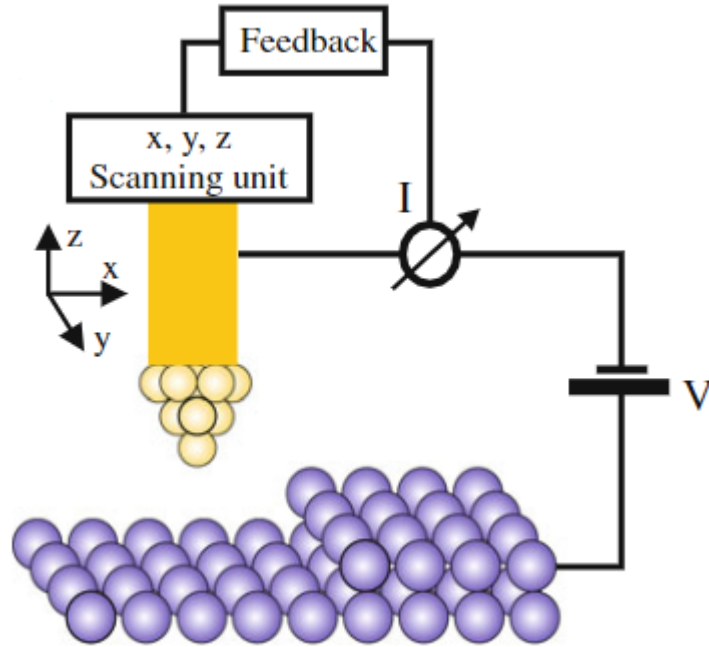
Figure 19: Schematic of an STM used on a sample consisting of 1 atom type. The sample has an elevation of one atomic layer on the right. A voltage V is applied between the probe and the sample. This figure has been extracted from Ref. [11].

4.1 Constant-current method

There are two ways of using the STM: a constant-current and a constant-height method. To obtain a height map of the sample, we move the probe over the surface and adjust the height of the probe to keep the current constant. This is done using piezoelectric actuators, which expand when an electric field is applied to them. For example, in Fig. 19, as the probe comes across the elevation in the sample, the tunnelling current will increase. This is used to activate the actuators, which raise the probe until the current returns to its original value. The height of the probe is then recorded as a function of the position of the probe, to produce an image of the surface, called a topograph, see Fig. 20. This will not always result in a perfect height map, since different atoms and molecules have different electronic properties that affect the tunnelling current. Some molecules can even inhibit the flow of electrons when added on the surface, causing the probe to lower as it passes over it. In any case, it will give us a very detailed map of the electronic
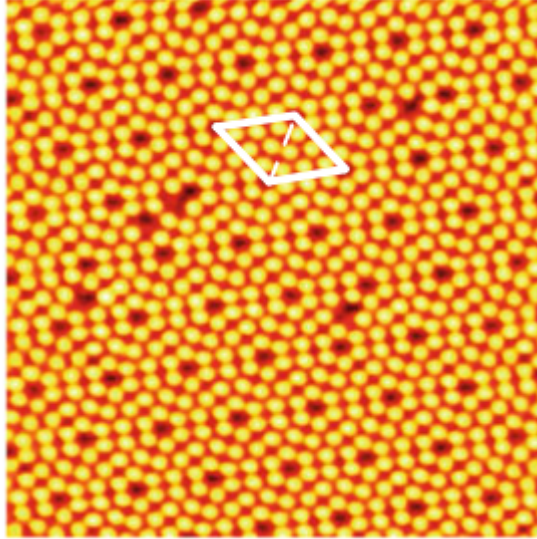
26

conductance at every part of the surface.

Figure 20: A topograph of a Si(111) surface. We can see that the resolution is good enough to distinguish individual Si-atoms, indicated by the yellow dots. We can also observe defects in the form of missing atoms. The unit cell has been highlighted by the white rhombus. This figure has been extracted from Ref. [11].

We will now quickly illustrate why we can generate a topograph with such precision. In general, the probability density of an electron with energy E at a position $\vec{r}$ is given by $|\psi(\vec{r})|^2$, where $\psi(\vec{r})$ is the wave function of the electron. For simplicity, let us consider a free electron in 1D. The probability density of the electron will then be homogeneous: $|\psi(z)|^2 = $ constant. If we now introduce a potential at $z = 0$ with a width d and height $V > E$, the electron will have a probability of tunnelling through the potential barrier, see Fig. 21. In general, the wave function decays exponentially in the barrier, hence we can write

$$\psi(z) \approx \psi(0)e^{-kz}, \text{ with } k = \sqrt{\frac{2m_e(V - E)}{\hbar^2}}, \text{ for } 0 < z < d. \quad (11)$$

Hence, the probability of an electron tunnelling through the barrier is given by the transmission coefficient T, with

$$T = \frac{|\psi(d)|^2}{|\psi(0)|^2} \approx e^{-2kd}. \quad (12)$$

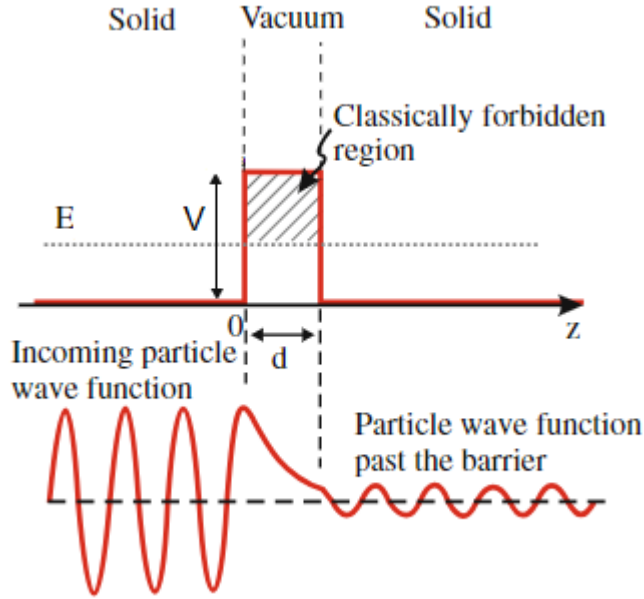The tunnelling current will therefore be proportional to this coefficient T.

27

Figure 21: Schematic overview of the quantum tunnelling of a free electron with energy E through a potential of height V and width d. The top figure shows the position of the potential, with the electron initially localized on the left. The bottom figure shows the exponential decay of the real part of its wave function when it tunnels through the potential. This figure has been extracted from Ref. [11].

This is essentially what happens when the electrons tunnel into the metal probe: the transmission coefficient exponentially decreases as the tip-sample distance increases. If we fill in some typical value for the energy difference $V - E \approx 4.5$ eV, we find that $2k \approx 22$ nm^{-1}. Therefore, if we increase the tip-sample distance by $\delta = 1$ Å, the transmission coefficient becomes about 9 times smaller: $T_d/T_{d+\delta} = \exp(2k\delta) \approx 9$. It now becomes clear why an STM can measure surface structures so accurately, since even a 1 Å protrusion, which is about the size of an atom, changes the current by an order of magnitude.

4.2 Constant-height method

Hence, the constant-current method gives us a very accurate to examine the topography of the sample. To actually get a sense of the LDOS, we need to measure the differential conductance dI/dV. This tells us the change in the current flowing through the metal tip as we increase the voltage between

the tip and the surface, and in order to measure this accurately, we keep the height of the probe fixed. As the voltage increases, it will be possible for lower energy electrons to bridge the tip-sample gap. Thus, if we look at $dI(V_0)/dV$ for a certain voltage V_0, we see the increase in the number of electrons that are now able to reliably cross the gap for this voltage. It would make sense to assume that this value is approximately proportional to the LDOS of the electrons at $E = eV_0$. However, we have shown that the transmission coefficient T depends exponentially on the square root of the voltage, see Eq. 12. This adds a featureless slope of background to our measurements, which increases exponentially as we increase the voltage. To get rid of the noise, we need to normalize dI/dV by dividing it by the total conductance I/V. For the normalized differential conductance we can correctly assume

$$\text{LDOS}(eV) \propto \frac{dI/dV}{I/V}. \tag{13}$$

To obtain the energy spectrum we need to average the LDOS over the entire sample. From this we get a total density of states as a function of the voltage. Since the total density of states is proportional to the density of energy levels, this tells us what the energy spectrum roughly looks like.

4.3 Designing the lattice

Finally, we need to find an accurate way to approximate the lattices we are interested in, such that we can measure them using an STM. To effectively make use of an STM, we need a surface that conducts electricity. Therefore, a copper surface is usually used as a starting point. On the copper surface, the electrons are free to move, and act effectively as a 2D electron gas. We can now add other atoms or molecules to the copper surface to build an approximation of the lattice. We can do this by using an STM again. If we move the metal tip close enough, we can cause a stronger interaction between the tip and the targeted atom, which can be either a repulsive or attractive interaction. We can use this stronger interaction to either "push" or "pull" the atom to the desired position, depending on the interaction type. The ability to place individual atoms exactly where we want them gives unprecedented control over the design of the sample, and enables us to accurately build any lattice. Depending on the atom or molecule that we have placed, this will induce a positive or negative potential for the electrons. We can place the negative potentials at the site locations to attract the electrons, or we can use the positive potentials to "box in" the electrons at the site locations. A typical molecule that is used for these experiments is a CO-molecule, which induces a repulsive potential.

5   Experimental Discussion

Now that we possess the required knowledge about STM, we can take a look at some interesting experiments within this field. However, there have not been any experiments about the one dimensional Fibonacci quasicrystal yet. We will therefore first look at an experiment that uses STM to study the electronic properties of a graphene lattice. Secondly, we will discuss an experiment that detects the LDOS for a two-dimensional quasicrystal, namely the Penrose tiling.

5.1   Designing a graphene lattice with STM

First off all, we will discuss the 2012 experiment by Gomes et al. about the graphene lattice, see Ref. [4]. Graphene is a monolayer crystal of carbon atoms, arranged in a hexagonal pattern also known as the honeycomb lattice, see Fig. 22. It has been a subject of interest for years among physicists, due to its many uncommon properties like high heat- and electrical-conductivity, in addition to its incredible strength. The simplest theoretical model that accurately describes the graphene lattice is the two-site tight-binding approximation with a single hopping parameter t. This model is simulated in the experiment using the technique described in the previous section. A structure similar to the graphene lattice is obtained by placing CO-molecules on the copper surface, following the pattern of the triangular Bravais-lattice, see Fig. 22.
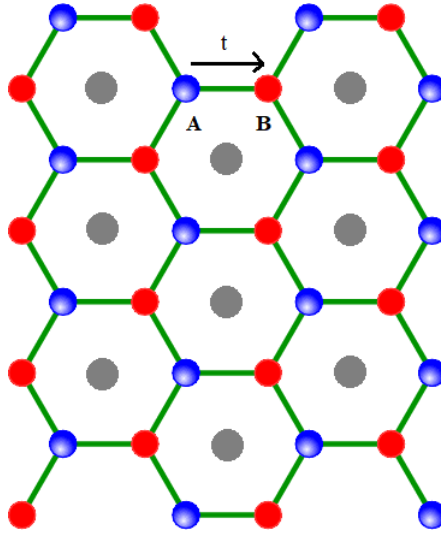
Figure 22: The graphene lattice. It consists of a single layer of carbon atoms, arranged in a honeycomb pattern. We can generate this lattice by taking a hexagonal Bravais-lattice, and then splitting every site into two new sites A and B. We then apply a nearest neighbour approximation with a certain hopping parameter t. The lattice can be simulated by placing CO-molecules at the positions of the grey dots.

Using STM, we can then look at the topograph for a specific voltage, and at the differential conductance for a certain voltage interval, see Fig. 23. In Fig. 23a, we can clearly see the honeycomb pattern and the effects at the edges of the lattice. In Fig. 23b, the spatially averaged differential conductance spectrum is shown. In essence, this is the spatially averaged LDOS on the interval $V = -200$ mV to $V = 200$ mV. Since every eigenstate corresponds to an energy eigenvalue at which it is most prominent, this shows us the approximate shape of the energy spectrum. Notice that there is no large gap in between the two peaks. Instead there seems to be a linear decrease after the first peak at E_M until the point E_D, after which the conductance seems to increase linearly again until the second peak. We now look at the energy spectrum in reciprocal space in the inset of the second figure. This reveals a double conical structure that reflects the linear dispersion relation between the two peaks and the minimum point that connects them. This shape is called a *Dirac cone* and the minimum E_D the *Dirac point*. The Dirac cone has long been theoretically predicted to appear in graphene, and is one of its main characteristics. Both metals and insulators have parabolic energy spectra in reciprocal space instead of conical; metals have a partially filled upper band and insulators possess a gap between the upper and lower band.

31

Thus, graphene does not fall within either of those categories. As a result of the Dirac cone, the electrons act as if they would be massless and therefore move with a constant Fermi velocity $v_F \approx c/300$ ms^{-1}. The existence of massless fermions in a graphene lattice had been reported experimentally by Novoselov et al., see Ref. [12].
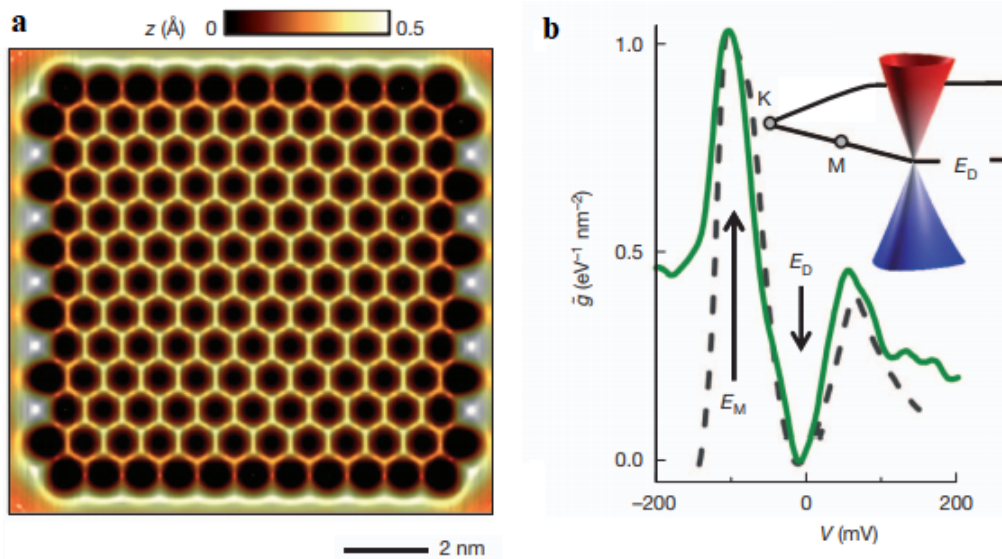

Figure 23: **a** The STM topograph for a lattice with 271 CO-molecules for $V = 10$ mV and $I = 1$ nA, with a lattice constant of $d = 8.8$ Å. **b** The differential conductance averaged over a number of sites near the centre of the lattice. The curve has been normalized by showing the ratio between the measured differential conductance and the differential conductance of a clean copper surface. The point E_M shows the maximum conductance at $V = -104$ mV, corresponding to the M-point in reciprocal space. The point E_D shows the minimum conductance at $V = -5$ mV, and corresponds to the Dirac point in reciprocal space. Furthermore, it is accompanied by a tight-binding, next-nearest neighbours fit, shown by the dashed line as a comparison. The inset shows the resulting Dirac-cone in reciprocal space. This figure has been extracted from Ref. [4].

5.2 Electronic properties of the Penrose Crystal

The second experiment aims to employ STM to study the LDOS of the quasicrystal corresponding to the Penrose tiling, where every vertex is a lattice site. Since the Penrose crystal is a two-dimensional quasicrystal, it is very well suited to be investigated with an STM, where we build the lattice on a

2D copper surface. The construction is shown in Fig. 24a. Before we look at the results of the experiment, let us quickly discuss the link with the Fibonacci quasicrystal. At first order, i.e. if we only look at nearest neighbours, the Fibonacci quasicrystal has two types of sites: atomic and molecular. We predicted that, despite the lack of translational symmetry, the LDOS and the energy spectrum still possess some order in relation to the different sites. We observed a threefold splitting of the energy eigenstates, where the upper and lower group of states were highly localized on the molecular sites, and the middle group highly localized on the atomic sites. It will now be interesting to see whether the lattice corresponding to the Penrose tiling expresses the same properties. In contrast to the Fibonacci crystal, the Penrose crystal actually has eight structurally different sites, see Fig. 24b.
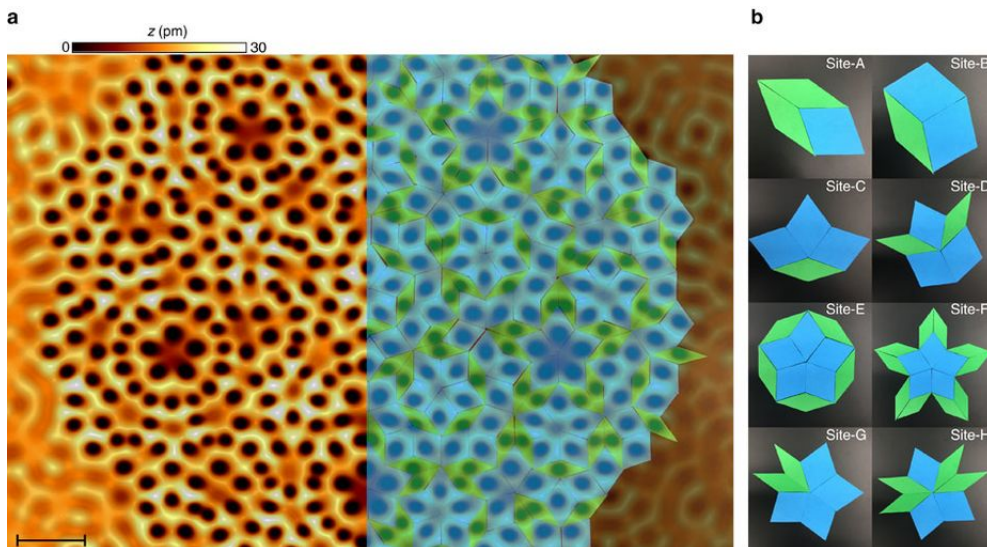

Figure 24: **a** The construction of the Penrose lattice. The left half of the figure shows the electron conductance at $V = 10$ mV and $I = 1$ nA. On the right hand side, an overlay of the Penrose tiling has been added. **b** The eight structurally different sites. The site in question is always at the centre. Every one of them has a different first order-structure, except for site-E and site-F, which are only different when comparing next-nearest neighbours (second order). However, the sites are formed by different matching rules, and should therefore be individually classified. This figure has been extracted from Ref. [5].

Now that we have the necessary information about the Penrose lattice, it is time to look at the differential conductance map for a couple of energy values, see Fig. 25a-c. Similar to the first experiment, the differential conductance

has been normalized by dividing it by the differential conductance of a clean copper surface. In Fig. 25d-f, we have highlighted different types of sites in the Penrose lattice. If we look at the conductance maps, we can see that for every voltage the electrons form a standing wave, but only at particular sites. For example, if we compare Fig. 25a to Fig. 25d, we notice that the standing wave is mainly localized on the B-sites. We see a similar localization on specific site types when we compare Fig. 25b,c to Fig. 25e,f, respectively. For $V = -200$ mV, the E-,G- and H-sites seem to be dominant, while for $V = -100$ mV, the F-sites are very clearly visible.
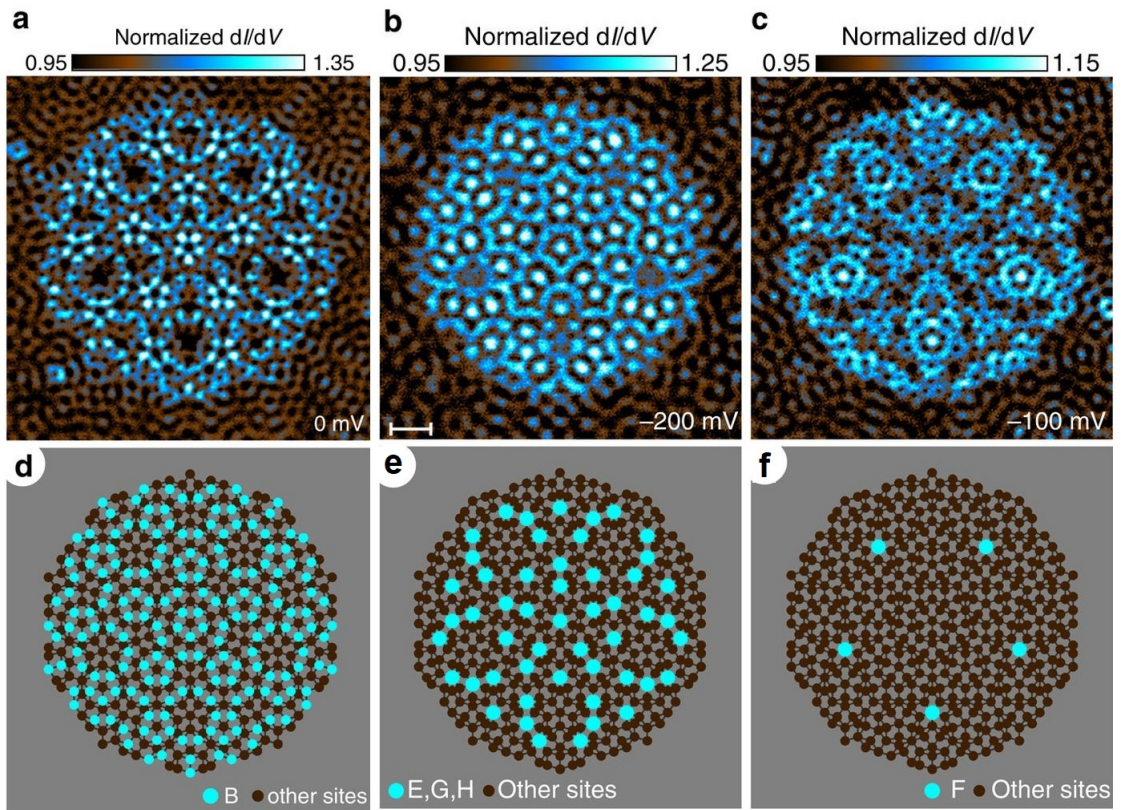

Figure 25: **a,b,c** The normalized conductance maps for $V = 0$, -200 and -100 mV. **d,e,f** The Penrose lattice sites, where certain site types have been highlighted in cyan for comparison. This figure has been extracted from Ref. [5].

To support this further, we also show the average normalized differential conductance for each of the site types as a function of the voltage, see Fig. 26. For comparison, we show the different site types again in Fig. 26a, and the differential conductance curves corresponding to these sites in Fig. 26b. No-

tice that each curve has its own peak at a certain voltage, supporting the claim that the states are grouped together at different energy values, and are localized on sites of a specific type. In Fig. 26c, we have shown the normalized conductance averaged over all sites. As expected for quasicrystals, it seems spiky and irregular.
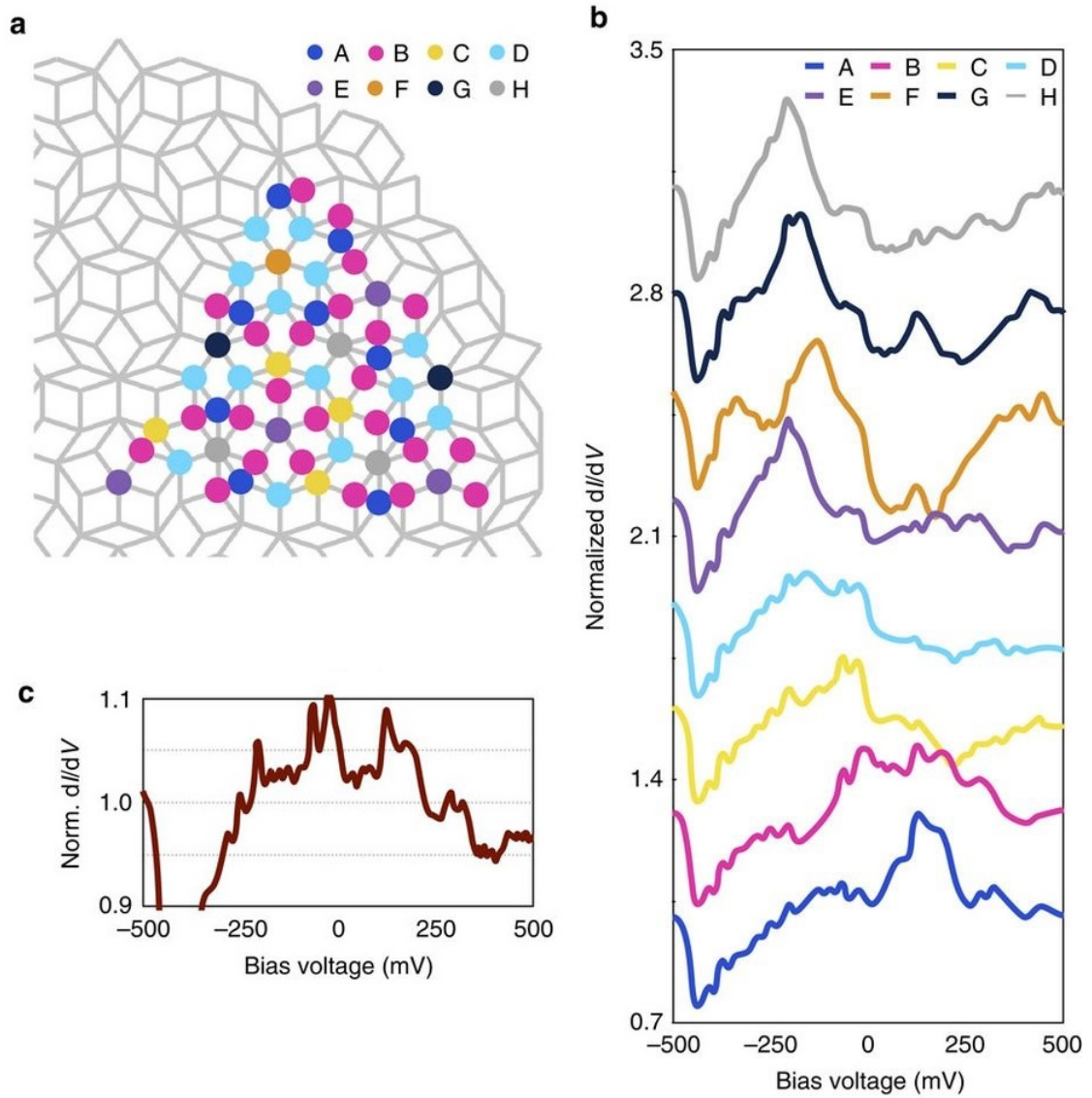
Figure 26: **a** The Penrose tiling with the different site types highlighted. **b** The normalized conductance curves for each of different site types. The conductance has been averaged over all sites of the same type near the centre of the lattice, to minimize edge effects. **c** The normalized conductance averaged over all sites. This figure has been extracted from Ref. [5].

In conclusion, despite the lack of periodicity, we still observe resonant states, which are localized at specific site types. This is very similar to the theoretical predictions about the Fibonacci quasicrystal we made in previous sections.

6 Conclusion

In this thesis we have explored quasicrystals, and in particular the mathematical properties of the Fibonacci quasicrystal.

In the first section, we discussed the discovery of quasicrystals in 1982 by Dan Shechtman, when he observed a diffraction pattern with 5-fold symmetry. We proved that any periodic lattice needs to have 2-, 3-, 4- or 6-fold rotational symmetry, which is what made Shechtman's discovery so surprising. We also introduced the projection method, with which quasicrystals can be generated from higher dimensional regular crystals. When we use this method to project a part of the 2D square lattice on a line with a slope equal to the golden ratio, we obtain the Fibonacci quasicrystal.

In the second section, we explained how the same quasicrystal can be constructed by making use of the Fibonacci word. At first order, this crystal has two different sites: molecular and atomic. We then showed that we can decompose its Hamiltonian into two molecular parts (bonding and antibonding) and one atomic part. From this we derived that its energy spectrum has a recursive structure, where it can be indefinitely divided into three parts, similar to a Cantor set. The eigenstates corresponding to the atomic energy levels are localized on the atomic sites, and idem for the molecular eigenstates. When we rearranged the sites according to their position in the 2D square lattice from which the quasicrystal is generated, the same three-fold symmetry emerged in the LDOS.

In the third section, we verified whether our predictions could be confirmed through numerical calculations. We solved the Schrödinger equation numerically 1D and 2D to simulate the Fibonacci quasicrystal, using potentials of different heights to replicate the different hopping parameters of the crystal. In the 1D model, we found a remarkable agreement with the theoretical predictions. The recursive structure is visible until two levels deep in the energy spectrum, and the same splitting is visible in the LDOS. The 2D offered similar results, but the recursive structure is less clear.

In the fourth section, we analysed Scanning Tunnelling Microscopy. This technique enables us to move around individual atoms on a conductive surface with atomic precision, therefore making it possible to design surfaces which accurately simulate 1D or 2D lattices. We can then measure their electronic properties by moving a probe very closely over the surface, and measure the current generated by the electrons that quantum tunnel into

the probe. By doing this for different voltages between the probe and the surface, we can obtain an accurate image of the energy spectrum and the localization of the eigenstates of the surface.

In the fifth and final section, we discussed two experiments that employ STM. The first experiment shows that it can successfully construct a surface which replicates a graphene lattice. Among others, the characteristic Dirac cone was observed in the energy spectrum. The second experiment investigates the 2D quasicrystal called the Penrose tiling. At first order, this crystal has eight structurally different sites. It was found that the eigenstates are somewhat clustered in groups, each of which seems to be localized on their own type of site. This is similar the Fibonacci quasicrystal, where molecular and atomic eigenstates are localized respectively on atomic and molecular sites.

It will be interesting to see if the predicted properties do emerge if an experiment of the Fibonacci quasicrystal is conducted. A clever surface would have to be designed, since our numerical calculations make use of perfectly rectangular potentials of different heights, and different boundary conditions, which are difficult to realize experimentally. Furthermore, it might be interesting to analyse the 5D crystal from which the Penrose tiling can be generated. In the Fibonacci quasicrystal, the site types corresponded with their position in the 2D ancestor crystal, which allowed us to rearrange the sites in a natural way, and we could find something similar for the Penrose crystal. The observation that we can categorize the sites according to their first-order structure, and that the states cluster in groups which are localized on specific site types could even be a general propery of quasicrystals, and could be a subject of a future study.

In conclusion, the Fibonacci quasicrystal has shown to possess some very interesting mathematical properties, which seem to hold up in numerical calculations. These properties have not been tested experimentally yet, but an experiment of a 2D quasicrystal shows similar properties.

References

[1] T. Janssen, *Aperiodic crystals: A contradictio in terminis?*, Phys. Rep. **168** (1988) 55-113

[2] Yaacov E. Kraus, Yoav Lahini, Zohar Ringel, Mor Verbin, and Oded Zilberberg, *Topological States and Adiabatic Pumping in Quasicrystals*, Phys. Rev. Lett. **109**, 106402 (2012)

[3] Nicolas Macé, Anuradha Jagannathan, and Frédéric Piéchon, *Fractal dimensions of wave functions and local spectral measures on the Fibonacci chain*, Phys. Rev. B **93**, 205153 (2016)

[4] Kenjiro K. Gomes, Warren Mar, Wonhee Ko, Francisco Guinea and Hari C. Manoharan, *Designer Dirac fermions and topological phases in molecular graphene*, Nature **483**, pages 306-310 (2012)

[5] Laura C. Collins, Thomas G. Witte, Rochelle Silverman, David B. Green and Kenjiro K. Gomes, *Imaging quasiperiodic electronic states in a synthetic Penrose tiling*, Nature Communications **8**, 15961 (2017)

[6] B. D. Cullity, *Elements of X-Ray Diffraction* (Addison-Wesley, Reading, Massachusetts, 1956), pp. 29

[7] Takanori Tsutaoka, Tomohito Tokunaga, Takashi Umeda and Toshinobu Maehara, *Observation of the two-dimensional reciprocal lattice by use of lattice grating sheets and a laser pointer*, Eur. J. Phys. **35** (2014) 055021 (11pp)

[8] D. Shechtman, I. Blech, D. Gratias and J. W. Cahn, *Metallic Phase with Long-Range Orientational Order and No Translational Symmetry*, Phys. Rev. Lett **53**, 1951 (1984)

[9] Hong-ru Ma and Chien-Hua Tsai, *On the energy spectra of one-dimensional quasi-periodic systems*, J. Phys. C: Solid State Phys. **21**, 4311-4324 (1988)

[10] Frédéric Piéchon, Mourad Benakli, and Anuradha Jagannathan, *Analytical Results for Scaling Properties of the Spectrum of the Fibonacci Chain*, Phys. Rev. Lett. **74**, 5248 (1995)

[11] Bert Voigtländer, *Scanning Probe Microscopy*, (Springer-Verlag, Berlin Heidelberg, 2015), pp. 1-11, 313-316, and 349-354

[12] K. S. Novoselov, A. K. Geim, S. V. Morozov, D. Jiang, M. I. Katsnelson, I. V. Grigorieva1, S. V. Dubonos and A. A. Firsov, *Two-dimensional gas of massless Dirac fermions in graphene*, Nature **438**, pages 197-200 (2005)

Appendix

**The Mathematica notebook used for the numerical calculations.**

```
(*The notebook that was used to simulate
 the 1D Fibonacci quasicrystal in 1D and 2D.*)
```

```
(*
The parameters that were used
 -α is the generation of the chain we want to simulate
 -fib is the α-th Fibonacci number, and therefore the number of sites
 -VL and VS are the potential heights
 -pwidth is half of the potential width
 -msite is the molecular site shrinking factor, called γ in the thesis
 -yheight is half of the width of the sites
*)
α = 10;
fib = Fibonacci[α];
VL = 50;
VS = 25;
pwidth = 0.1;
msite = 0.94;
yheight = 0.4;
(*We then calculate the number of molecular and atomic sites
 (nmols and natoms) and the total length of the lattice (lattlength)*)
nmols = Fibonacci[α - 2];
natoms = Fibonacci[α - 3];
lattlength = msite * 2 * nmols + natoms;
(*We generate the Fibonacci word. It is generated by making use of the conumbers,
in order to make sure every site always has the
 correct conumber assigned. By generating it this way,
the Fibonacci word and therefore the lattice can sometimes be shifted,
but this does not influence any of the outcomes*)
conumbers = ReplacePart[Table[Mod[Fibonacci[α - 1] * i, fib], {i, 1, fib}], -1 → fib];
permutation = Table[Position[conumbers, i][[1, 1]], {i, 1, Length[conumbers]}];
A = Table[, {i, 1, fib}];
For[i = 2, i ≤ fib, i++,
  If[conumbers[[i]] > Fibonacci[α - 2] && conumbers[[i]] ≤ Fibonacci[α - 1],
    {A[[i]] = L, A[[i - 1]] = L},]];
A[[1]] = L; A[[-1]] = L;
For[i = 2, i < fib, i++, If[A[[i]] === Null,
  If[A[[i + 1]] === Null && A[[i - 1]] === S, A[[i]] = L, A[[i]] = S],]]
A = Prepend[A, L];
(*We calculate the permutated positions*)
dist = Table[If[A[[i]] === L && A[[i - 1]] === L, 1, msite], {i, 2, Length[A]}];
pos = Prepend[Table[Sum[dist[[j]], {j, 1, i}], {i, 1, Length[dist]}], 0];
pospermutation = Table[pos[[permutation[[i]] + 1]], {i, 1, fib}];
(*We define the potential function*)
B2 = Table[{If[A[[n]] === S, VS, VL],
    Abs[x - pos[[n]]] < pwidth && y ≥ -yheight && y ≤ yheight}, {n, 1, Length[A]}];
Z[x_, y_] := Piecewise[B2];
(*Finally, we numerically solve the Schrödinger equation*)
{vals2, funs2} = NDEigensystem[
   {-Laplacian[u[x, y], {x, y}] + Z[x, y] * u[x, y],
    DirichletCondition[u[x, y] == 0, (y ≥ yheight || y ≤ -yheight)],
    PeriodicBoundaryCondition[u[x, y], x == 0 && (y < yheight && y > -yheight),
     TranslationTransform[{lattlength, 0}]]},
      u, {x, 0, lattlength}, {y, -yheight, yheight}, fib,
   Method → {"SpatialDiscretization" →
```

```
        {"FiniteElement", "MeshOptions" → {"MaxCellMeasure" → 0.01}}}];
(*We plot the eigenvalues*)
eigenvaluesplot = ListPlot[Table[vals2[[n]], {n, 1, fib}],
  PlotRange → Full, AxesLabel → {"index", "energy"}, Frame → True]
```

Out[311]=
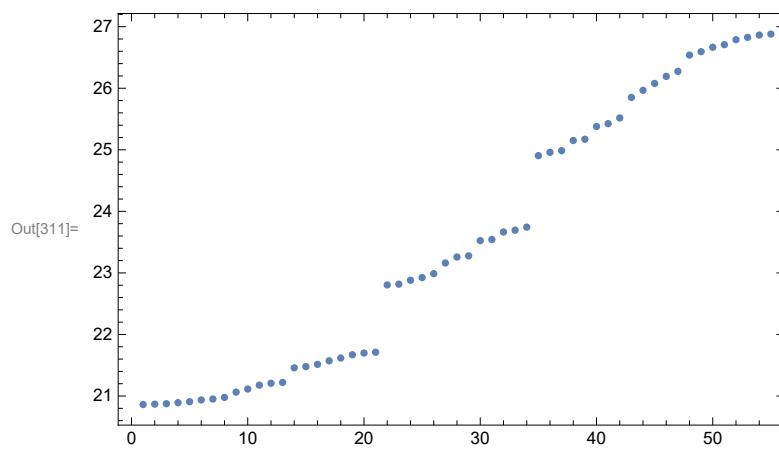
```
(*We now want to calculate the LDOS. Based on the spacing of the energy values we
   determine a value for the standard deviation σ. We then define the LDOS-function*)
σ = 0.2;
LDOS2[x_, y_, ϵ_] :=
   Sum[Abs[funs2[[n]][x, y]]^2 * PDF[NormalDistribution[vals2[[n]], σ], ϵ], {n, fib}];
(*We define the position permutation function*)
mhalf = msite nmols;
diff = nmols - mhalf;
poschange[x_] :=
   Piecewise[{{pospermutation[[Ceiling[x/msite]]] - msite + x - msite Floor[x/msite],
      x ≤ mhalf && x > 0}, {pospermutation[[Ceiling[x + diff]]] - 1 +
      x - (mhalf + Floor[x - mhalf]), x > mhalf && x ≤ mhalf + natoms},
     {pospermutation[[Ceiling[(x - natoms)/msite + natoms]]] - msite + x -
       (natoms + msite Floor[(x - natoms)/msite]), x > mhalf + natoms && x ≤ lattlength}}];
(*We plot the LDOS for the permutated sites*)
conumberplot2 = DensityPlot[LDOS2[poschange[x], 0, ϵ],
   {x, 0.01, fib - 1.01}, {ϵ, Floor[vals2[[1]]], Ceiling[vals2[[fib]]]},
   PlotPoints → 100, Frame → True, FrameLabel → {"conumbers", "energy levels"}]
```
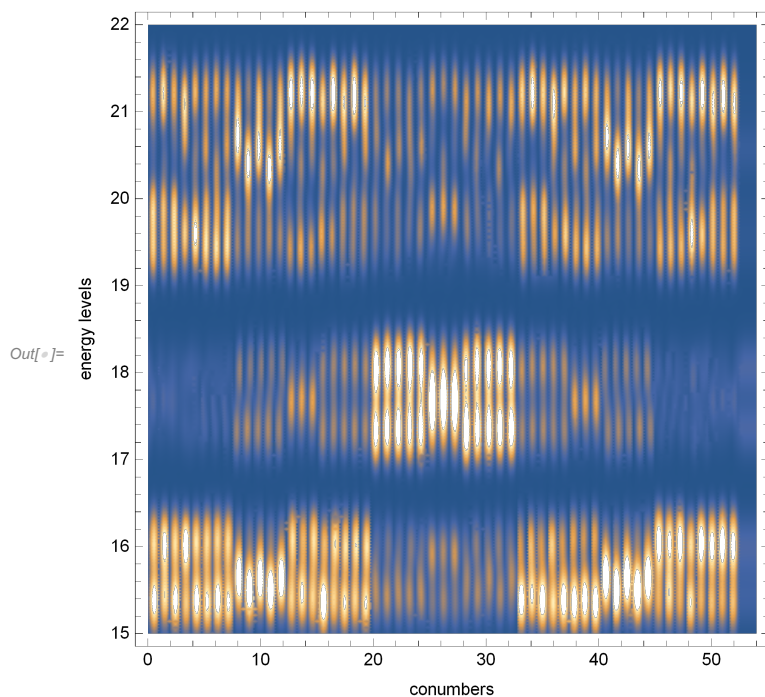
Out[ ]=


```
(*We now do the exact same, but in 1D*)
```

```
In[312]:= α = 10;
        fib = Fibonacci[α];
        VL = 50;
        VS = 25;
        pwidth = 0.1;
        nmols = Fibonacci[α - 2];
        natoms = Fibonacci[α - 3];
        msite = 0.94;
        lattlength = msite * 2 * nmols + natoms;

        conumbers = ReplacePart[Table[Mod[Fibonacci[α - 1] * i, fib], {i, 1, fib}], -1 → fib];
        permutation = Table[Position[conumbers, i][[1, 1]], {i, 1, Length[conumbers]}];
        A = Table[, {i, 1, fib}];
        For[i = 2, i ≤ fib, i++,
          If[conumbers[[i]] > Fibonacci[α - 2] && conumbers[[i]] ≤ Fibonacci[α - 1],
            {A[[i]] = L, A[[i - 1]] = L},]];
        A[[1]] = L; A[[-1]] = L;
        For[i = 2, i < fib, i++, If[A[[i]] === Null,
          If[A[[i + 1]] === Null && A[[i - 1]] === S, A[[i]] = L, A[[i]] = S],]]
        A = Prepend[A, L];

        dist = Table[If[A[[i]] === L && A[[i - 1]] === L, 1, msite], {i, 2, Length[A]}];
        pos = Prepend[Table[Sum[dist[[j]], {j, 1, i}], {i, 1, Length[dist]}], 0];
        pospermutation = Table[pos[[permutation[[i]] + 1]], {i, 1, fib}];

        B1 = Table[{If[A[[n]] === S, VS, VL], Abs[x - pos[[n]]] < pwidth}, {n, 1, Length[A]}];
        W[x_] := Piecewise[B1];
        {vals, funs} = NDEigensystem[
            {-Laplacian[u[x], {x}] + W[x] * u[x],
              PeriodicBoundaryCondition[u[x], x == 0, TranslationTransform[{lattlength}]]},
                u, {x, 0, lattlength}, 2 fib, Method → {"SpatialDiscretization" →
              {"FiniteElement", "MeshOptions" → {"MaxCellMeasure" → 0.01}}}];

        eigenvaluesplot = ListPlot[Table[vals[[n]], {n, 1, fib}],
          PlotRange → {{0, fib + 1}, {Floor[vals[[1]]], Ceiling[vals[[fib]]]}},
          AxesLabel → {"index", "energy"}, Frame → True]
```
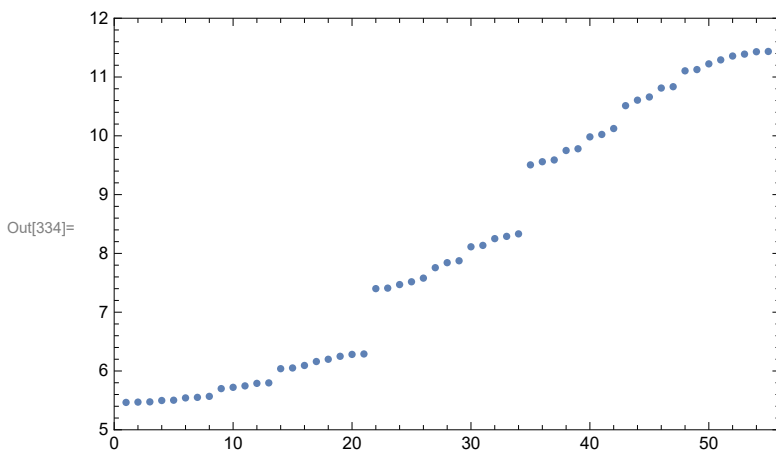
Out[334]=

```
In[278]:= σ = 0.1;
LDOS[x_, ϵ_] :=
  Sum[Abs[funs[[n]][x]]^2 * PDF[NormalDistribution[vals[[n]], σ], ϵ], {n, fib}];

mhalf = msite nmols;
diff = nmols - mhalf;
poschange[x_] :=
  Piecewise[{{pospermutation[[Ceiling[x/msite]]] - msite + x - msite Floor[x/msite],
      x ≤ mhalf && x > 0}, {pospermutation[[Ceiling[x + diff]]] - 1 +
      x - (mhalf + Floor[x - mhalf]), x > mhalf && x ≤ mhalf + natoms},
     {pospermutation[[Ceiling[(x - natoms)/msite + natoms]]] - msite + x -
       (natoms + msite Floor[(x - natoms)/msite]), x > mhalf + natoms && x ≤ lattlength}}];


conumberplot = DensityPlot[LDOS[poschange[x], ϵ],
  {x, 0.01, lattlength}, {ϵ, Floor[vals[[1]]], Ceiling[vals[[fib]]]},
  PlotPoints → 100, Frame → True, FrameLabel → {"conumbers", "energy levels"}]
```